Enhanced Structure–Function Relationship in Glaucoma With an Anatomically and Geometrically Accurate Neuroretinal Rim Measurement

Vishva M. Danthurebandara,[1] Glen P. Sharpe,[1] Donna M. Hutchison,[1] Jonathan Denniss,[2,3] Marcelo T. Nicolela,[1] Allison M. McKendrick,[2] Andrew Turpin,[3] and Balwantray C. Chauhan[1]

[1]Department of Ophthalmology and Visual Sciences, Dalhousie University and Capital Health District Authority, Halifax, Nova Scotia, Canada
[2]Department of Optometry and Vision Sciences, University of Melbourne, Victoria, Australia
[3]Department of Computing and Information Systems, University of Melbourne, Victoria, Australia

Correspondence: Balwantray C. Chauhan, Department of Ophthalmology and Visual Sciences, Dalhousie University, 1276 South Park Street, 2W Victoria, Halifax, NS, Canada B3H 2Y9; bal@dal.ca.

Submitted: July 31, 2014
Accepted: November 24, 2014

Citation: Danthurebandara VM, Sharpe GP, Hutchison DM, et al. Enhanced structure–function relationship in glaucoma with an anatomically and geometrically accurate neuroretinal rim measurement. *Invest Ophthalmol Vis Sci*. 2015;56:98–105. DOI:10.1167/iovs.14-15375

Purpose. To evaluate the structure–function relationship between disc margin–based rim area (DM-RA) obtained with confocal scanning laser tomography (CSLT), Bruch's membrane opening–based horizontal rim width (BMO-HRW), minimum rim width (BMO-MRW), peripapillary retinal nerve fiber layer thickness (RNFLT) obtained with spectral-domain optical coherence tomography (SD-OCT), and visual field sensitivity.

Methods. We examined 151 glaucoma patients with CSLT, SD-OCT, and standard automated perimetry on the same day. Optic nerve head (ONH) and RNFL with SD-OCT were acquired relative to a fixed coordinate system (acquired image frame [AIF]) and to the eye-specific fovea-BMO center (FoBMO) axis. Visual field locations were mapped to ONH and RNFL sectors with fixed Garway-Heath (VF_{GH}) and patient-specific (VF_{PS}) maps customized for various biometric parameters.

Results. Globally and sectorally, the structure–function relationships between DM-RA and VF_{GH}, BMO-HRW_{AIF} and VF_{GH}, and BMO-HRW_{FoBMO} and VF_{PS} were equally weak. The R^2 for the relationship between DM-RA and VF_{GH} ranged from 0.1% (inferonasal) to 11% (superotemporal) whereas that between BMO-HRW_{AIF} and VF_{GH} ranged from 0.1% (nasal) to 10% (superotemporal). Relatively stronger global and sectoral structure–function relationships with BMO-MRW_{AIF} and with BMO-MRW_{FoBMO} were obtained. The R^2 between BMO-MRW_{AIF} and VF_{GH} ranged from 5% (nasal) to 30% (superotemporal), whereas that between BMO-MRW_{FoBMO} and VF_{PS} ranged from 5% (nasal) to 25% (inferotemporal). The structure–function relationship with RNFLT was not significantly different from that with BMO-MRW, regardless of image acquisition method.

Conclusions. The structure–function relationship was enhanced with BMO-MRW compared with the other neuroretinal rim measurements, due mainly to its geometrically accurate properties.

Keywords: glaucoma, structure–function relationship, optic nerve head, visual field, automated perimetry

Glaucoma is progressive optic neuropathy diagnosed on the basis of functional damage, structural damage, or both. Functional damage is established most commonly with the presence of visual field loss, whereas structural damage is established with loss of the neuroretinal rim of the optic nerve head (ONH) or the retinal nerve fiber layer (RNFL). Because of the lack of a universally accepted definition of glaucoma, the use of either mode of diagnosis presumes there is a meaningful correlation between functional and structural damage in glaucoma. However, previous investigations have shown that this relationship is modest at best.[1–5]

Current ONH examination includes an assessment of the neuroretinal rim width, conventionally the distance between the clinically defined optic disc margin and the cup edge. However, recent investigations explain how anatomic and geometric errors in disc margin–based evaluation result in inaccurate rim measurements.[6,7] Bruch's membrane opening (BMO), identified readily with spectral-domain optical coherence tomography (SD-OCT), has been recognized as a reliable and consistent border of the rim, and BMO-derived rim measurements have been proposed.[6–15] Furthermore, several investigators have recognized the importance of taking rim tissue orientation, relative to the point of measurement, into account.[6,8,11,12,16,17] In our recent reports we introduced an index, BMO-minimum rim width (BMO-MRW),[7,16] which quantifies the rim from its actual anatomical border and also accounts for its variable orientation. This index has proven to have better diagnostic accuracy for glaucoma than conventional rim measurements.[11,16]

Typically, ONH images are acquired and regionalized relative to fixed horizontal and vertical axes of the acquired image frame (AIF) of the imaging device. However, the position of the

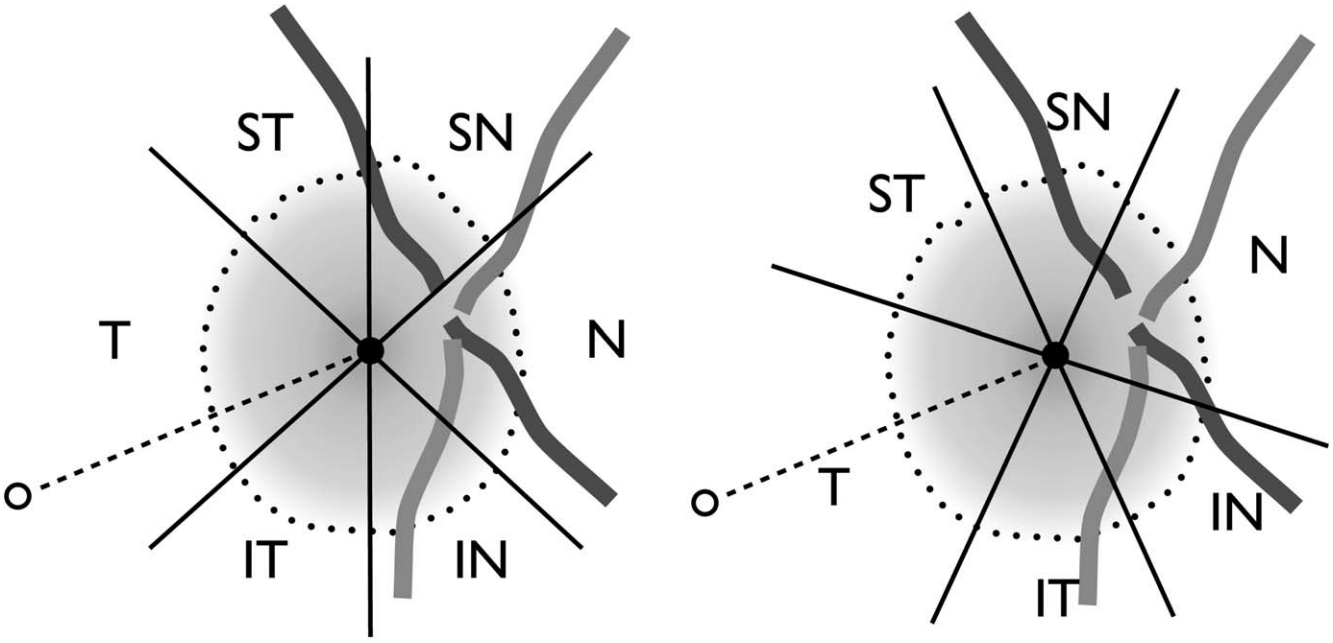

FIGURE 1. Impact of regionalizing neuroretinal rim relative to the FoBMO axis. (*Left*) Current regionalization according to positions that are fixed relative to the imaging frame of the imaging device resulting in rim measurements from variably different anatomical locations. (*Right*) Regionalization according to the patient-specific FoBMO axis ensuring that the neuroretinal rim width in a given sector refers the same anatomical location among different individuals. *Dots*, BMO; *open circle*, fovea; *filled circle*, BMO center. IN, inferonasal; IT, inferotemporal; N, nasal; SN, superonasal; ST, superotemporal; T, temporal.

fovea relative to BMO, quantified by the angle between the fovea and the BMO center relative to the horizontal axis of the image acquisition frame, termed the fovea-BMO center (FoBMO) axis, varies by as much as 20°.[6,18] Due to this large interindividual variation, rim measurements in a given ONH sector do not precisely refer to the same anatomical location among different individuals, potentially resulting in artificially large interindividual variation in sectoral rim measurements and errors in mapping the visual field to ONH sectors (Fig. 1). Therefore, image acquisition and regionalization relative to the patient-specific FoBMO axis could be important in allowing more meaningful comparisons between individuals. In most previous studies, visual field locations were mapped to ONH sectors according to the population-average visual field maps proposed by Garway-Heath et al.[19] Recently, Turpin et al.[20] and Denniss et al.[21–23] proposed a computational model to derive patient-specific visual field maps that take into account individual differences in several important anatomical parameters. These individualized approaches may have a bearing on the structure–function relationship.

Because of the new refinements in rim quantification, logical methods of image acquisition, and individualized visual field mapping, we undertook this study to reexplore the structure–function relationship. We examined the change in the relationship from the current disc margin–based rim measurements with AIF image acquisition and Garway-Heath visual field maps, to BMO-derived rim measurements obtained with FoBMO acquisition and individualized visual field maps.

METHODS

Participants

A total of 151 glaucoma patients were recruited from two ongoing longitudinal observational studies at the Eye Care Centre, Queen Elizabeth II Health Science Centre, Halifax, Nova Scotia, Canada. Each patient had standard automated perimetry (24-2 SITA standard strategy,[24] Humphrey Field Analyzer; Carl Zeiss Meditec, Dublin, CA, USA), confocal scanning laser tomography (CSLT) (Heidelberg Retina Tomograph [HRT]; Heidelberg Engineering GmbH, Heidelberg, Germany), and SD-OCT (Spectralis; Heidelberg Engineering GmbH) performed on the same day. Inclusion criteria were as follows: visual field damage characteristic of open angle glaucoma, with mean deviation between −2 and −10 dB, when first recruited for the longitudinal studies; clinical appearance of glaucomatous cupping and/or localized notching of the neuroretinal rim; best corrected visual acuity ≥6/12; and pupil diameter ≥3 mm. Exclusion criteria were as follows: nonglaucomatous ocular disease and systemic disease or systemic medication known to affect the visual field or ability to participate in the study; chronic ocular medication other than for glaucoma; distance refraction not exceeding 5.00 diopters equivalent sphere and 3.00 diopters of astigmatism; and contact lens wear. The study adhered to the tenets of the Declaration of Helsinki, and all patients gave written, informed consent. If both eyes were eligible, one eye was randomly selected as the study eye. The study was approved by the Capital Health Ethics Review Board.

Image Acquisition

The ONH was imaged with CSLT and SD-OCT, and the peripapillary RNFL was imaged with SD-OCT.

Confocal scanning laser tomography acquires three, three-dimensional 15° scans with transverse sampling of 384 × 384 pixels and with 16 images per millimeter of scan depth.[25] A mean topography image is computed with the three images. Rim area is one of the several ONH parameters derived from CSLT after the operator defines the clinically visible optic disc margin (DM). As such, this rim parameter will be referred to as the DM-based rim area (DM-RA). Global and regional DM-RA values depend on the position of the HRT reference plane that

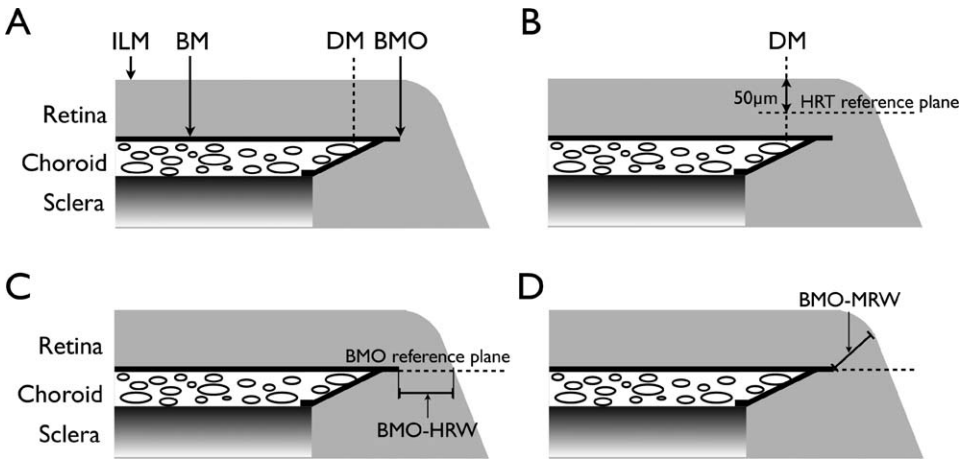

Figure 2. Schematic representations of the DM and the BMO-derived neuroretinal rim parameters. (**A**) Anatomical representation. (**B**) Representation of the HRT reference plane 50 µm below the ILM at the temporal DM between 350° and 356°. (**C**) Representation of the BMO reference plane and BMO-HRW, the distance from BMO to the ILM along the BMO reference plane. (**D**) Representation of BMO-MRW, the minimum distance from BMO to the ILM irrespective of the plane.

is fixed 50 µm below the temporal surface of the DM (between 350° and 356°; Fig. 2B).[26]

Spectral-domain OCT images of the ONH were acquired and sectorized relative to (1) the fixed horizontal and vertical axes of the AIF (AIF acquisition, which also includes AIF sectorization) and (2) the individuals' FoBMO axis (FoBMO acquisition, which also includes FoBMO sectorization).

In AIF acquisition, the operator centered the image frame approximately on the ONH. Two scan patterns were used: a radial pattern with 24 high-resolution 15° radial scans, each averaged from 20 to 30 individual B-scans, with 1536 A-scans per B-scan acquired with scanning speed of 40,000 A-scans per second; and a circular scan along a peripapillary circle of 3.5 mm diameter to measure RNFL thickness. Once the images were acquired, in each radial B-scan, the BMO points and internal limiting membrane (ILM) were identified and marked by an automated algorithm and corrected when necessary.[27] The BMO-derived rim parameters have been detailed elsewhere[7,16]; however, briefly, the BMO-horizontal rim width (BMO-HRW) was defined as the distance between BMO and ILM along the BMO reference plane, and BMO-MRW was defined as the minimum distance between BMO and ILM. Both parameters measure the rim from an anatomically identifiable location; however, only BMO-MRW takes the variable rim tissue orientation into account (Figs. 2C, 2D).

Table 1. Structural Parameters of Interest and Their Anatomical and Geometrical Differences

	Anatomy	Geometry	
Parameter	Outer Rim Margin	MRW/HRW	Image Acquisition Method
DM-RA	DM	N/A	N/A
$BMO\text{-}HRW_{AIF}$	BMO	HRW	AIF
$BMO\text{-}HRW_{FoBMO}$	BMO	HRW	FoBMO
$BMO\text{-}MRW_{AIF}$	BMO	MRW	AIF
$BMO\text{-}MRW_{FoBMO}$	BMO	MRW	FoBMO
$RNFLT_{AIF}$	N/A	N/A	AIF
$RNFLT_{FoBMO}$	N/A	N/A	FoBMO

Anatomy includes identification of the outer rim margin; geometry includes MRW or HRW and the image acquisition method. N/A, not applicable.

In FoBMO acquisition, the operator identifies and marks the foveal pit and the four BMO points in two live B-scans initially at 45° and 135°. These live scans can be rotated to positions where the BMO points are most identifiable. Based on these initial marks, the image frame is adjusted according to FoBMO axis and the BMO position is approximated. Similar to AIF acquisition, 24 high-resolution radial scans and a circular scan along a peripapillary circle of 3.5-mm diameter were obtained. The BMO and ILM in each radial scan were identified in the same manner described for AIF acquisition and the same BMO-derived rim parameters were computed. The ONH and peripapillary RNFL images with CSLT and SD-OCT yielded seven structural parameters of interest. Table 1 summarizes the anatomical and geometrical differences between each parameter.

Structure–Function Mapping

The Garway-Heath visual field map[19] (VF_{GH}) is a widely used technique to map the topographic relationship between visual field locations and ONH sectors. Application of VF_{GH} assumes the same ocular anatomy among different individuals and hence the same visual field map is used for each individual.

We also used patient-specific visual field maps (VF_{PS}) that include certain ocular biometric parameters in the computation.[20–23] For each individual, the model relates each visual field location to 1° ONH sectors taking into account axial length, longitude and latitude of the center of the ONH, and horizontal and vertical ONH diameter. The model assumes that retinal ganglion cell axons course along the shortest available path around the spherical surface from the retinal ganglion cell body to ONH. To avoid axons crossing the fovea, papillomacular ONH sectors were considered to be filled once axons from the macular region were accounted for. The complete algorithm is detailed elsewhere.[20,21] Figure 3 illustrates VF_{GH} and VF_{PS} for three individuals whose FoBMO angles were 5.5°, –7.0°, and –15.5°, the largest positive, average, and most negative FoBMO angles of patients in the study, respectively. Sector averages of rim parameters were estimated at each degree around ONH with linear interpolation.

Because VF_{PS} maps account for FoBMO orientation, in the correlation analysis, VF_{PS} maps could be analyzed only with structural parameters determined with FoBMO acquisition. The DM-RA and the parameters measured in AIF acquisition

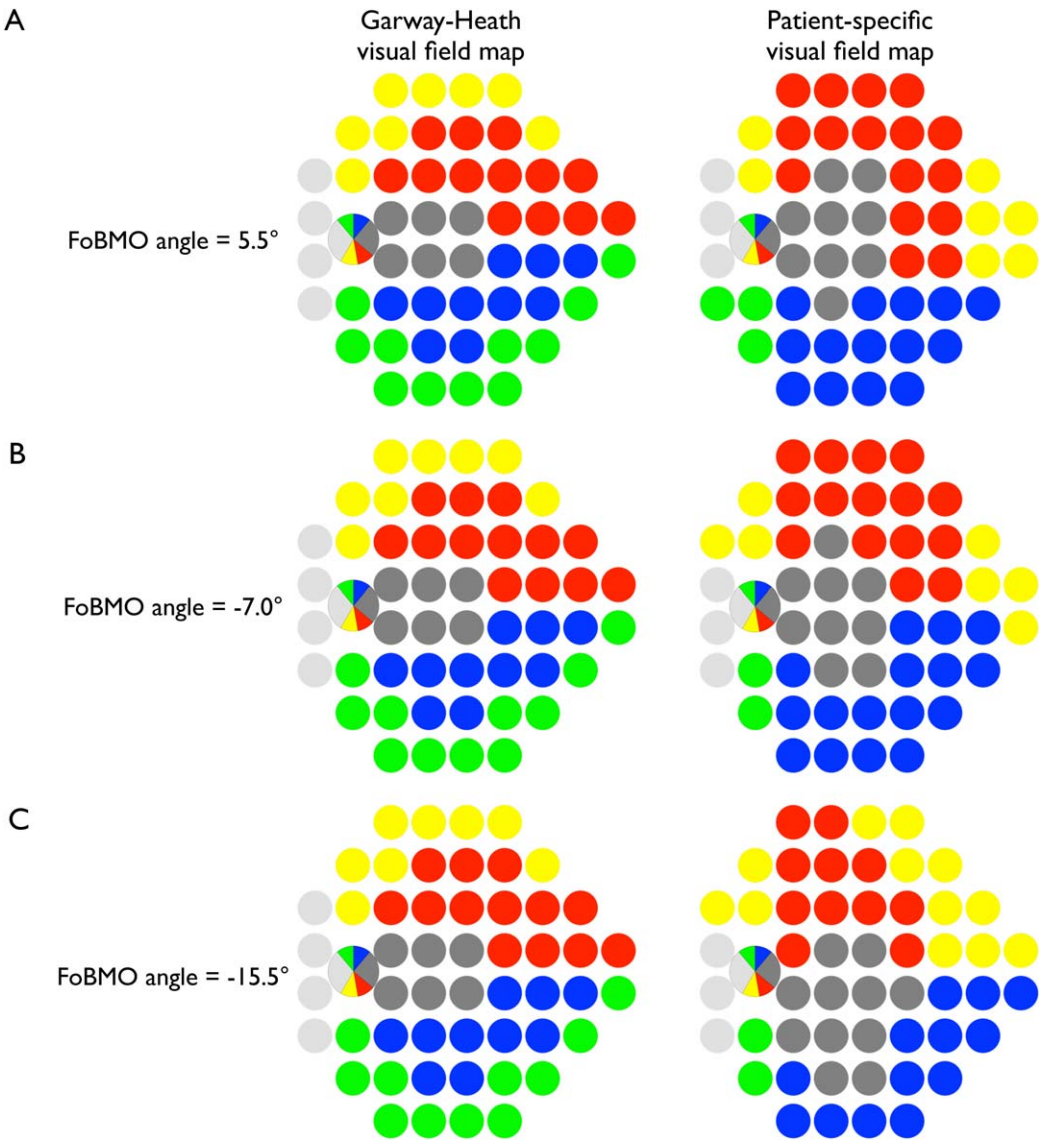

FIGURE 3. Difference between current VF_{GH} and VF_{PS}. (**A**) The VF_{GH} and VF_{PS} for an individual whose FoBMO angle was 5.5°, the most positive FoBMO angle of patients in the study. (**B**) An individual whose FoBMO angle was −7.0°, the average FoBMO angle of patients in the study. (**C**) An individual whose FoBMO angle was −15.5°, the most negative FoBMO angle of patients in the study.

were related to visual field sensitivities regionalized with the VF_{GH}.

Statistical Analysis

Visual field threshold values were expressed in 1/Lambert (linear scale; dB = 10 × $\log_{10}$ [1/Lambert]).[28,29] The relationship between global mean sensitivity (MS) and each of the global rim parameters, as well as that between the sectoral MS and the sectoral rim parameters, were assessed with linear regression. The strength of the relationship was evaluated with the coefficient of determination value (R^2) of each model. Pearson correlation coefficients also were calculated.

Strength of the structure–function relationship was categorized as a function of anatomy, geometry, and image acquisition method and each one was assessed from several different correlation comparisons that are summarized in Table 2. The correlations were not independent from each other, as they were calculated for the same set of patients. Hence, a comparison of dependent correlations with a common parameter, visual field sensitivity, (comparisons 1, 3, 4, 8, and 9 in Table 2) was assessed with Steiger's test,[30] whereas a comparison of dependent correlations with nonoverlapping parameters (comparisons 2, 5, 6, and 7 in Table 2) was assessed with the Raghunathan, Rosenthal, and Rubin's test.[31]

To examine the intraindividual variability of BMO-MRW differences due to the image acquisition method, we calculated the absolute relative difference (*ARD*) between $BMO\text{-}MRW_{AIF}$ and $BMO\text{-}MRW_{FoBMO}$ relative to $BMO\text{-}MRW_{AIF}$ (i.e., $ARD_{MRW} = abs\ (BMO\text{-}MRW_{AIF} - BMO\text{-}MRW_{FoBMO})/BMO\text{-}MRW_{AIF}$), measuring the degree of discordance between $BMO\text{-}MRW_{AIF}$ and $BMO\text{-}MRW_{FoBMO}$ relative to $BMO\text{-}MRW_{AIF}$ Interindividual variability of BMO-MRW also was examined.

Results

There were 151 glaucoma patients in the study whose median (interquartile range [IQR]) age was 71.3 (64.8–77.8) years. The

Table 2. Comparisons of Structure–Function Relationships

Comparison	Correlations Compared
Anatomy, DM vs. BMO	1. r (DM-RA, VF_{GH}) vs. r (BMO-HRW_{AIF}, VF_{GH})
	2. r (DM-RA, VF_{GH}) vs. r (BMO-HRW_{FoBMO}, VF_{PS})
Geometry, HRW vs. MRW	3. r (BMO-HRW_{AIF}, VF_{GH}) vs. r (BMO-MRW_{AIF}, VF_{GH})
	4. r (BMO-HRW_{FoBMO}, VF_{PS}) vs. r (BMO-MRW_{FoBMO}, VF_{PS})
Image acquisition, AIF vs. FoBMO	5. r (BMO-HRW_{AIF}, VF_{GH}) vs. r (BMO-HRW_{FoBMO}, VF_{PS})
	6. r (BMO-MRW_{AIF}, VF_{GH}) vs. r (BMO-MRW_{FoBMO}, VF_{PS})
	7. r ($RNFLT_{AIF}$, VF_{GH}) vs. r ($RNFLT_{FoBMO}$, VF_{PS})
BMO-MRW vs. RNFLT	8. r (BMO-MRW_{AIF}, VF_{GH}) vs. r ($RNFLT_{AIF}$, VF_{GH})
	9. r (BMO-MRW_{FoBMO}, VF_{PS}) vs. r ($RNFLT_{FoBMO}$, VF_{PS})

r, Pearson correlation coefficient.

median (IQR) visual field mean deviation was –3.6 (–7.7 to –1.7) dB. A summary of the global CSLT and SD-OCT parameters is shown in Table 3.

Global and sectoral R^2 values for the relationship between each structural parameter and corresponding visual field sensitivity are shown in Figure 4. The relationship between global DM-RA and global MS was weak ($R^2 = 0.01$, $P = 0.191$; Fig. 4A). Similarly, the relationship between global BMO-HRW_{AIF} and global MS ($R^2 = 0.01$, $P = 0.281$) and between global BMO-HRW_{FoBMO} and global MS ($R^2 = 0.02$, $P = 0.131$) was weak (Fig. 4B). On the other hand, both global BMO-MRW_{AIF} and global BMO-MRW_{FoBMO} were better associated with global MS ($R^2 = 0.14$ and 0.14, respectively, $P < 0.010$) compared with their BMO-HRW counterpart measurements (Fig. 4C). Likewise, the relationship between global retinal nerve fiber layer thickness with AIF acquisition ($RNFLT_{AIF}$) and global MS ($R^2 = 0.17$, $P < 0.001$) and between global $RNFLT_{FoBMO}$ and global MS ($R^2 = 0.15$, $P < 0.001$) was also stronger (Fig. 4D).

For each structural parameter, the strongest sectoral structure–function relationship was found in the inferotemporal sector. The R^2 for the relationship between inferotemporal BMO-MRW_{AIF} and corresponding MS was 0.27 ($P < 0.001$; Fig. 4C), whereas it was 0.25 ($P < 0.001$; Fig. 4C) between inferotemporal BMO-MRW_{FoBMO} and corresponding MS. Moreover, a strong relationship was found between the inferotemporal $RNFLT_{AIF}$ and corresponding MS ($R^2 = 0.42$, $P < 0.001$; Fig. 4D), as well as between the inferotemporal $RNFLT_{FoBMO}$ and corresponding MS ($R^2 = 0.34$, $P < 0.001$; Fig. 4D).

Table 3. Summary of Global ONH and RNFL Parameters of the Study Patients

Parameter	Median (IQR)
DM-RA, mm^2	0.96 (0.78–1.18)
BMO-HRW_{AIF}, μm	279.57 (202.72–355.05)
BMO-HRW_{FoBMO}, μm	257.55 (197.99–340.59)
BMO-MRW_{AIF}, μm	184.73 (153.03–220.54)
BMO-MRW_{FoBMO}, μm	182.97 (150.84–222.90)
$RNFLT_{AIF}$, μm	67.29 (61.24–77.47)
$RNFLT_{FoBMO}$, μm	67.81 (60.23–78.26)

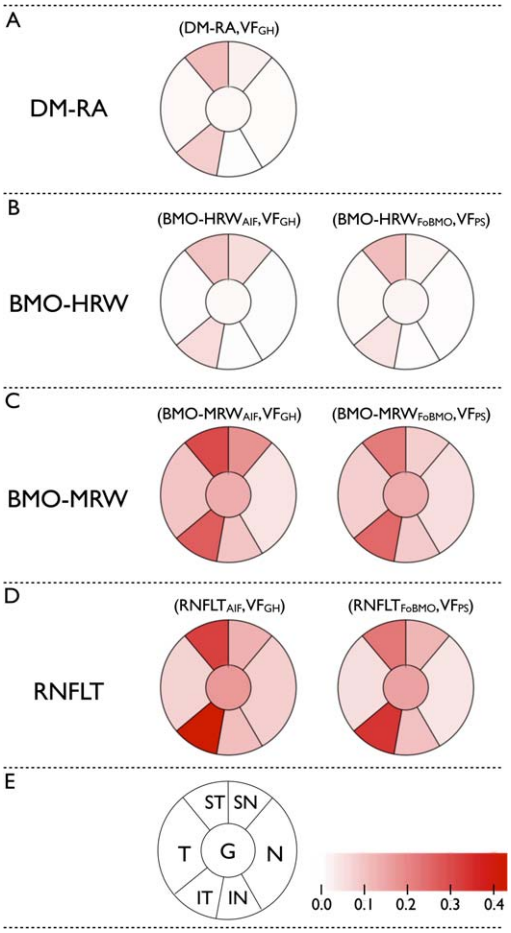

Figure 4. Coefficient of determination (R^2) values of global and sectoral structure–function relationships. (**A**) Between DM-RA and corresponding VF_{GH}. (**B**) Between BMO-HRW_{AIF} and VF_{GH} and between BMO-HRW_{FoBMO} and corresponding visual field sensitivity regionalized with VF_{PS}. (**C**) Between BMO-MRW_{AIF} and VF_{GH} and between BMO-MRW_{FoBMO} and VF_{PS}. (**D**) Between $RNFLT_{AIF}$ and VF_{GH} and between $RNFLT_{FoBMO}$ and VF_{PS}. (**E**) Figure legend: corresponding ONH sectors and the color scale representing R^2 values.

The P values from correlation comparisons in Table 2 are shown in Figure 5. The correlation between DM-RA and MS was not significantly different from that between BMO-HRW and MS with either AIF or FoBMO acquisition ($P > 0.100$, globally and in all sectors; Fig. 5A). However, globally and sectorally, the correlation between BMO-MRW and MS was significantly better than that between BMO-HRW and MS with either AIF or FoBMO acquisition ($P < 0.001$; Fig. 5B). Global or sectoral correlations with AIF acquisition were not significantly different from that with FoBMO acquisition, except in superior sectors with BMO-MRW ($P = 0.010$; Fig. 5C) and in inferotemporal sector with RNFLT ($P = 0.001$; Fig. 5C). In these particular sectors, structure–function correlations with AIF acquisition were stronger than with FoBMO acquisition. Moreover, largely similar sectoral structure–function relationships were obtained with BMO-MRW and RNFLT, regardless the image acquisition method (Fig. 5D).

The distribution of sectoral BMO-MRW with the two acquisition methods is shown in Supplementary Figure S1. The unsigned median difference between BMO-MRW_{FoBMO} and BMO-MRW_{AIF} (Supplementary Fig. S1) ranged from 1.5 μm (temporal) to 11 μm (superonasal). However, the IQR of BMO-MRW_{FoBMO} and BMO-MRW_{AIF} (Supplementary Fig. S1) ranged

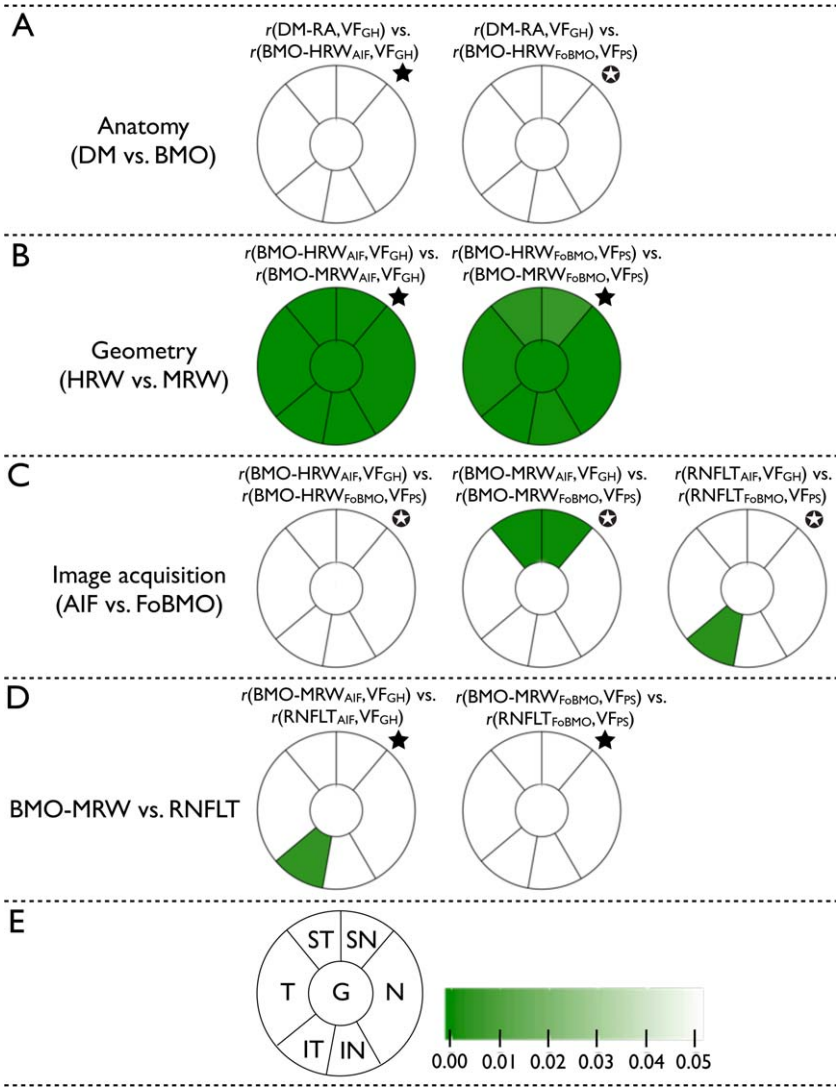

Figure 5. *P* values from Steiger's★ or Raghunathan, Rosenthal, and Rubin's tests✪ for the nine comparisons of the structure–function correlations shown in Table 2. (**A**, *left*) Between DM-RA and corresponding VF_{GH}, and BMO-HRW_{AIF} and VF_{GH}. (**A**, *right*) Between DM-RA and VF_{GH}, and BMO-HRW_{FoBMO} and corresponding visual field sensitivity regionalized with VF_{PS}. (**B**, *left*) Between BMO-HRW_{AIF} and VF_{GH}, and BMO-MRW_{AIF} and VF_{GH} (significant *P* values are in favor of BMO-MRW_{AIF}). (**B**, *right*) Between BMO-HRW_{FoBMO} and VF_{PS}, and BMO-MRW_{FoBMO} and VF_{PS} (significant *P* values are in favor of BMO-MRW_{FoBMO}). (**C**, *left*) Between BMO-HRW_{AIF} and VF_{GH}, and BMO-HRW_{FoBMO} and VF_{PS}. (**C**, *middle*) Between BMO-MRW_{AIF} and VF_{GH}, and BMO-MRW_{FoBMO} and VF_{PS} (significant *P* values are in favor of BMO-MRW_{AIF}). (**C**, *right*) Between $RNFLT_{AIF}$ and VF_{GH}, and $RNFLT_{FoBMO}$ and VF_{PS} (significant *P* values are in favor of $RNFLT_{AIF}$). (**D**, *left*) Between BMO-MRW_{AIF} and VF_{GH}, and $RNFLT_{AIF}$ and VF_{GH}. (**D**, *right*) Between BMO-MRW_{FoBMO} and VF_{PS}, and $RNFLT_{FoBMO}$ and VF_{PS}. (**E**) Figure legend: corresponding ONH sectors and the color scale representing *P* values.

from 61.9 μm (temporal) to 115.8 μm (inferotemporal), and from 61.9 μm (temporal) to 108.4 μm (inferotemporal), respectively. Depending on sector, the number of patients who showed more than 20% difference between BMO-MRW_{AIF} and BMO-MRW_{FoBMO}, relative to BMO-MRW_{AIF}, ranged from 0 (0%, nasal; Supplementary Fig. S2) to 23 (15.2%, inferotemporal; Supplementary Fig. S2). Globally, 58 (38%) patients showed more than 20% difference between BMO-MRW_{AIF} and BMO-MRW_{FoBMO} at least in one ONH sector. These data illustrate that although the interindividual difference in BMO-MRW estimates based on image acquisition methods was small, the intraindividual difference could be considerable.

Discussion

Examination of the relationship between structural and functional loss in glaucoma could help to optimize and individualize structural and functional tests for diagnosing and monitoring glaucoma.[28] Although a robust relationship between test results of these two procedures would be expected, surprisingly, it is modest at best.[1–5] This study evaluated changes in the structure–function relationship obtained by taking into account some recent developments in imaging methods, in the clinical assessment of the ONH, and in visual field mapping.

Since the advent of SD-OCT, it has been proposed by some groups that BMO should be a consistent anatomical landmark from which neuroretinal rim measurements should be made.[6–15] The BMO-derived rim parameters we used quantify the rim from an actual anatomical border, however, only BMO-MRW takes the variable rim tissue orientation at the point of measurement into account, thus avoiding overestimation of rim width when the path of axons is more parallel to the horizontal plane. The effect of these anatomical and geomet-

rical changes in the clinical assessment of ONH on the structure–function relationship was examined. Our study also was designed to allow evaluation of the combined effect of image acquisition method, which compared the fixed AIF and individualized FoBMO image acquisition and sectorization, as well as the fixed VF_{GH} and individualized VF_{PS} visual field mapping, which may help to disclose the true structure–function relationship.[21,23,32–34]

Global and sectoral structure–function relationships with DM-RA, BMO-HRW_{AIF}, and BMO-HRW_{FoBMO} were equally weak. However, relatively stronger global and sectoral relationships were obtained with BMO-MRW_{AIF} and BMO-MRW_{FoBMO}. It is important to note the consistently weaker global and sectoral relationships with BMO-HRW compared with BMO-MRW, regardless of the image acquisition method. The geometric accuracy of BMO-MRW compared with BMO-HRW is likely the reason why higher correlations were obtained with BMO-MRW. These results are compatible with the recent findings on glaucoma detection based on various rim parameters that show that although DM-RA and BMO-HRW had comparable diagnostic accuracy, they were consistently poorer than BMO-MRW.[11,16]

Global and sectoral structure–function relationships with RNFLT were significantly stronger than those with DM-RA and BMO-HRW. Higher correlations with RNFLT compared with DM-RA have been reported previously[1,4,5]; however, to the best of our knowledge, there are no published reports that have compared the structure–function relationships with BMO-derived rim parameters and with RNFLT using both AIF and FoBMO image acquisition methods.

Global or sectoral correlations with AIF acquisition and VF_{GH} were not significantly different from those with FoBMO acquisition and VF_{PS}, except in the superior sectors with BMO-MRW and in the inferotemporal sector with RNFLT (Fig. 5C). Further analyses showed that these significant results were due to some extreme sectoral visual field sensitivity averages, which were artificially generated with individualized mapping. Individualized visual field mapping applied to data from current clinical tests yields a varying number of locations per sector because the visual field test pattern is invariable (Fig. 3). For example, the VF_{GH} maps 11 visual field locations to the superonasal ONH sector, whereas the VF_{PS} mapped fewer than 4 locations in the same ONH sector for 104 (69%) study patients. The nasal sector of VF_{GH} maps four locations to the nasal ONH sector; however, VF_{PS} mapped fewer than four locations in 121 (80%) patients. When a given patient has few individually mapped visual field locations for a particular ONH sector, together with high visual field sensitivity at those locations, the average sensitivity for that sector would be higher compared with that with the fixed VF_{GH} map and have an impact on the corresponding structure–function correlation. Patient-specific mapping may be expected to result in better structure–function correlations in eyes with extreme FoBMO orientations. We examined the sectoral structure–function correlation between BMO-MRW and corresponding visual field sensitivity values for patients whose FoBMO orientation was less than −10°. However, results from this analysis remained similar to the original analysis.

To our surprise, we observed only a minor effect of image acquisition method and individualized ONH and RNFL sectorization on the structure–function relationship in the population in spite of the fact that the FoBMO angle can vary by as much as 20°. This finding is likely due to the large interindividual variability of structural parameters. For example, the population difference in mean BMO-MRW due to image acquisition method is much smaller compared with its interindividual difference with either acquisition method. Correlation models take into account only the variability among individuals; therefore, at the population level, we found that the impact of image acquisition method was relatively small, in agreement with the recent findings of He et al.[18] However, the discordance between BMO-MRW_{AIF} and BMO-MRW_{FoBMO} at the individual level is substantial. Fifty-eight (38%) patients had more than 20% difference between BMO-MRW_{AIF} and BMO-MRW_{FoBMO} in at least one ONH sector. Therefore, although the effect of image acquisition method on the structure–function relationship is minor at the population level, it might have a clinically important effect at the individual level.

Individualized visual field mapping yields a varying number of locations per sector. Figure 3 shows that some sectors are highly undersampled with the 24-2 pattern, particularly in the superonasal and inferonasal sectors where structure–function relationships would be imprecise. On the other hand, the superotemporal and inferotemporal sectors showed the strongest relationships, as they were comparatively well sampled relative to the superonasal and inferonasal sectors. Therefore, at the population level, individualized mapping might not have much of an impact on the structure–function relationship. However, for a given patient, individualized mapping remains constant and therefore might have a significant benefit in the follow-up of individual patients and elucidating the relationship between structural and functional changes.

Due to the design setting of the study, only a combined effect of visual field mapping and image acquisition method could be assessed. That is, for example, the true effect of image acquisition method alone cannot be determined because calculating the correlation between BMO-MRW_{FoBMO} and VF_{GH} is not possible, as the regionalization of the visual field is not corrected for the individual's FoBMO orientation. Therefore, visual field sensitivities regionalized with the VF_{GH} were related only with structural parameters determined with AIF acquisition.

In conclusion, current DM-based rim assessment, which lacks a reasonable anatomic and geometric rationale, showed an expected weak structure–function correlation. In spite of an anatomically accurate measurement, BMO-HRW also was weakly associated with corresponding visual field sensitivity, most likely because it is geometrically inaccurate. The BMO-MRW is both an anatomically and geometrically accurate rim measurement,[7,8,12,17] and resulted in a higher correlation with visual field sensitivity, comparable to that with the RNFL. Our results indicate that the most significant source (anatomy, geometry, image acquisition method, and visual field mapping) of the improvement in the structure–function relationship is the geometric correction that accounts for the variable rim tissue orientation at the point of measurement.

Acknowledgments

Supported by Grants MOP11357 (BCC) from the Canadian Institutes of Health Research, Ottawa, Ontario; unrestricted research support from Heidelberg Engineering (BCC), Heidelberg, Germany; and Grant LP130100055 from the Australian Research Council (AMM, AT).

Disclosure: **V.M. Danthurebandara**, None; **G.P. Sharpe**, None; **D.M. Hutchison**, None; **J. Denniss**, None; **M.T. Nicolela**, None; **A.M. McKendrick**, Heidelberg Engineering (F); **A. Turpin**, Heidelberg Engineering (F); **B.C. Chauhan**, Heidelberg Engineering (F, R)

References

1. Bowd C, Zangwill LM, Medeiros FA, et al. Structure-function relationships using confocal scanning laser ophthalmoscopy,

optical coherence tomography, and scanning laser polarimetry. *Invest Ophthalmol Vis Sci*. 2006;47:2889–2895.
2. Gardiner SK, Johnson CA, Cioffi GA. Evaluation of the structure-function relationship in glaucoma. *Invest Ophthalmol Vis Sci*. 2005;46:3712–3717.
3. Gardiner SK, Ren R, Yang H, Fortune B, Burgoyne CF, Demirel SA. Method to estimate the amount of neuroretinal rim tissue in glaucoma: comparison with current methods for measuring rim area. *Am J Ophthalmol*. 2014;157:540–549.
4. Nilforushan N, Nassiri N, Moghimi S, et al. Structure-function relationships between spectral-domain OCT and standard achromatic perimetry. *Invest Ophthalmol Vis Sci*. 2012;53:2740–2748.
5. Rao HL, Zangwill LM, Weinreb RN, Leite MT, Sample PA, Medeiros FA. Structure-function relationship in glaucoma using spectral-domain optical coherence tomography. *Arch Ophthalmol*. 2011;129:864–871.
6. Chauhan BC, Burgoyne CF. From clinical examination of the optic disc to clinical assessment of the optic nerve head: a paradigm change. *Am J Ophthalmol*. 2013;156:218–227.e2.
7. Reis AS, O'Leary N, Yang H, et al. Influence of clinically invisible, but optical coherence tomography detected, optic disc margin anatomy on neuroretinal rim evaluation. *Invest Ophthalmol Vis Sci*. 2012;53:1852–1860.
8. Chen TC. Spectral domain optical coherence tomography in glaucoma: qualitative and quantitative analysis of the optic nerve head and retinal nerve fiber layer (an AOS thesis). *Trans Am Ophthalmol Soc*. 2009;107:254–281.
9. Hu Z, Abramoff MD, Kwon YH, Lee K, Garvin MK. Automated segmentation of neural canal opening and optic cup in 3D spectral optical coherence tomography volumes of the optic nerve head. *Invest Ophthalmol Vis Sci*. 2010;51:5708–5717.
10. Mwanza JC, Oakley JD, Budenz DL, Anderson DR. Ability of cirrus HD-OCT optic nerve head parameters to discriminate normal from glaucomatous eyes. *Ophthalmology*. 2011;118:241–248.e1.
11. Pollet-Villard F, Chiquet C, Romanet JP, Noel C, Aptel F. Structure-function relationships with spectral-domain optical coherence tomography retinal nerve fiber layer and optic nerve head measurements. *Invest Ophthalmol Vis Sci*. 2014;55:2953–2962.
12. Povazay B, Hofer B, Hermann B, et al. Minimum distance mapping using three-dimensional optical coherence tomography for glaucoma diagnosis. *J Biomed Opt*. 2007;12:041204.
13. Reis AS, Sharpe GP, Yang H, Nicolela MT, Burgoyne CF, Chauhan BC. Optic disc margin anatomy in patients with glaucoma and normal controls with spectral domain optical coherence tomography. *Ophthalmology*. 2012;119:738–747.
14. Strouthidis NG, Yang H, Fortune B, Downs JC, Burgoyne CF. Detection of optic nerve head neural canal opening within histomorphometric and spectral domain optical coherence tomography data sets. *Invest Ophthalmol Vis Sci*. 2009;50:214–223.
15. Strouthidis NG, Yang H, Reynaud JF, et al. Comparison of clinical and spectral domain optical coherence tomography optic disc margin anatomy. *Invest Ophthalmol Vis Sci*. 2009;50:4709–4718.
16. Chauhan BC, O'Leary N, Almobarak FA, et al. Enhanced detection of open-angle glaucoma with an anatomically accurate optical coherence tomography-derived neuroretinal rim parameter. *Ophthalmology*. 2013;120:535–543.
17. Strouthidis NG, Fortune B, Yang H, Sigal IA, Burgoyne CF. Longitudinal change detected by spectral domain optical coherence tomography in the optic nerve head and peripapillary retina in experimental glaucoma. *Invest Ophthalmol Vis Sci*. 2011;52:1206–1219.
18. He L, Ren R, Yang H, et al. Anatomic vs. acquired image frame discordance in spectral domain optical coherence tomography minimum rim measurements. *PLoS One*. 2014;9:e92225.
19. Garway-Heath DF, Poinoosawmy D, Fitzke FW, Hitchings RA. Mapping the visual field to the optic disc in normal tension glaucoma eyes. *Ophthalmology*. 2000;107:1809–1815.
20. Turpin A, Sampson GP, McKendrick AM. Combining ganglion cell topology and data of patients with glaucoma to determine a structure-function map. *Invest Ophthalmol Vis Sci*. 2009;50:3249–3256.
21. Denniss J, McKendrick AM, Turpin A. An anatomically customizable computational model relating the visual field to the optic nerve head in individual eyes. *Invest Ophthalmol Vis Sci*. 2012;53:6981–6990.
22. Denniss J, Turpin A, McKendrick AM. Individualized structure-function mapping for glaucoma: practical constraints on map resolution for clinical and research applications. *Invest Ophthalmol Vis Sci*. 2014;55:1985–1993.
23. Denniss J, Turpin A, Tanabe F, Matsumoto C, McKendrick AM. Structure-function mapping: variability and conviction in tracing retinal nerve fibre bundles and comparison to a computational model. *Invest Ophthalmol Vis Sci*. 2014;55:728–736.
24. Heijl A, Patella VM, Bengtsson B. *Effective Perimetry*. Dublin, CA: Carl Zeiss Meditec, Inc.; 2012:1–9.
25. Fingeret M. Using the Heidelberg Retina Tomograph II (HRT II): image acquisition and accessing the data. In: Fingeret M, Flanagan JG, Liebmann JM, eds. *The Essential HRT Primer*. San Ramon, CA: Jocoto Advertising, Inc.; 2005:11–30.
26. Poli A, Strouthidis NG, Ho TA, Garway-Heath DF. Analysis of HRT images: comparison of reference planes. *Invest Ophthalmol Vis Sci*. 2008;49:3970–3975.
27. Almobarak FA, O'Leary N, Reis AS, et al. Automated segmentation of optic nerve head structures with optical coherence tomography. *Invest Ophthalmol Vis Sci*. 2014;55:1161–1168.
28. Hood DC, Kardon RH. A framework for comparing structural and functional measures of glaucomatous damage. *Prog Retin Eye Res*. 2007;26:688–710.
29. Garway-Heath DF, Caprioli J, Fitzke FW, Hitchings RA. Scaling the hill of vision: the physiological relationship between light sensitivity and ganglion cell numbers. *Invest Ophthalmol Vis Sci*. 2000;41:1774–1782.
30. Steiger J. Tests for comparing elements of a correlation matrix. *Psychol Bull*. 1980;87:245–251.
31. Raghunathan TE, Rosenthal R, Rubin DB. Comparing correlated but nonoverlapping correlations. *Psychological Methods*. 1996;1:178–183.
32. Jansonius NM, Nevalainen J, Selig B, et al. A mathematical description of nerve fiber bundle trajectories and their variability in the human retina. *Vision Res*. 2009;49:2157–2163.
33. Lamparter J, Russell RA, Zhu H, et al. The influence of intersubject variability in ocular anatomical variables on the mapping of retinal locations to the retinal nerve fiber layer and optic nerve head. *Invest Ophthalmol Vis Sci*. 2013;54:6074–6082.
34. Jansonius NM, Schiefer J, Nevalainen J, Paetzold J, Schiefer U. A mathematical model for describing the retinal nerve fiber bundle trajectories in the human eye: average course, variability, and influence of refraction, optic disc size and optic disc position. *Exp Eye Res*. 2012;105:70–78.

Investigative Ophthalmology & Visual Science